

INFLUENCE OF INGESTED GAS CROSSFLOW ON THE FORMATION AND STRUCTURE OF SECONDARY FLOWS IN THE BLADE PASSAGE OF A GAS TURBINE

K. N. Volkov

UDC 532.529

This paper considers the influence of the mass flow of the gas ingested from the cavity formed by the rotor-to-stator clearance on the formation and structure of secondary flows in the blade passage of the gas-turbine stage. The flow is described by the Reynolds-averaged Navier–Stokes equations, to close which the Spalart–Allmaras model and the k – ϵ model of turbulence with corrections for the rotation and curvature of the streamlines are used. Comparison of the results of the numerical simulation obtained from the point of view of different turbulence models is made.

Introduction. The tendency for an increase in the working-medium temperature at the inlet to the blade passage of the gas turbine to 1800–2000 K has made it necessary to provide proper cooling of the streamline surfaces. Of interest in solving the problem of cooling the blades of gas turbines is the interaction between the main stream in the blade passage and the crossflow of the gas ingested from the cavity formed by the rotor-to-stator clearance. The crossflow of the ingested gas leads to a change in the structure of the flow in the passage and additional losses of the total head. Therefore, we need information on the rate of flow of ingested gas that provides, on the one hand, the required cooling of the gas turbine blades and, on the other hand, the required indices of its efficiency.

Secondary flows are one of the main factors influencing the loss of the total head (up to 30%) and the increase in the heat flow to the walls of the blade passage [1, 2]. Secondary flows are formed in the vicinity of the surface formed by the intersection of the airfoil with the blade-passage walls as a result of the interaction between the horseshoe vortex formed upstream from the front edge of the airfoil and the vortex structures developing in the passage because of the airfoil surface curvature and the pressure gradient [3].

Traditionally, in many investigations the k – ϵ model is used to calculate the flow in the cavity and the Spalart–Allmaras model (or the mixing-length model) is used to calculate the flow in the blade passage [4–16].

The calculations of the flows in the cavity show that the k – ϵ model with near-wall functions and the two-level model of turbulence permit obtaining fairly accurate results [4]. The exception is the case of small Reynolds numbers, which is due to the limitations of the method of near-wall functions. The latter requires a larger number of mesh points, and in calculating geometrically complex flows, the problem of joining the external and internal subregions of the boundary layer arises. Comparison of the results obtained on the basis of different turbulence models, in particular, the Spalart–Allmaras model, the k – ϵ model, and the SST (Shear Stress Transport) model makes it possible to draw the conclusion that the choice of the eddy viscosity model is no importance in describing the flow in the cavity [5].

To calculate the flow in the blade passage, the mixing-length model [6] and the Spalart–Allmaras model [7], as well as the two-parameter turbulence models [8, 9] are widely used. To widen the range of their applicability, corrections for the rotation and curvature of the streamlines are used [8]. In [9], comparison of the Spalart–Allmaras model the SST model, and the V2F model as applied to the flow in the gas turbine stage is made. It is shown that the results of the numerical simulation depend on the choice of the turbulence model which is associated with the laminar–turbulent transition on the airfoil surface.

The data of numerical and physical experiments show that even comparatively low flow rates of the gas ingested from the cavity lead to the formation of a nonstationary flow in the blade passage [10–16]. In some cases, the

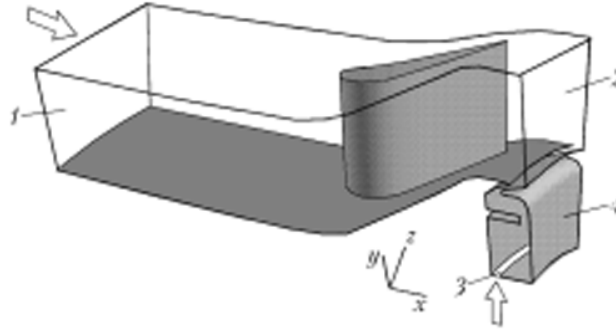


Fig. 1. Calculated region.

k - ϵ model gives results that agree with experiments [10, 11]. At the same time, in [12, 13] disagreement between experimental data and results of calculations with the use of the Spalart–Allmaras model is noted. The conclusions of [14, 15] show that to obtain accurate calculated data, one has to calculate simultaneously the flows in the blade passage and in the cavity.

In the present paper, numerical simulation of the flow in the blade passage of the gas turbine stage and in the cavity formed by the rotor-to-stator clearance has been performed. It has been shown that the ingested gas crossflow influences the formation and structure of the secondary flows in the blade passage, as well as the loss of the total head. To close the Reynolds-averaged Navier–Stokes equations, the Spalart–Allmaras model and the k - ϵ model with corrections for the rotation and curvature of the streamlines are used.

Basic Equations. The calculated region presented in Fig. 1 is bounded by the airfoil surface, the blade passage walls, the periodical surface (not shown in the figure), and the inlet 1 and outlet 2 passage boundaries, as well as by the inlet boundary 3 and walls 4 of the cavity.

In the Cartesian coordinate system (x, y, z) , the nonstationary flow of a viscous incompressible gas is described by the equation

$$\frac{\partial \mathbf{Q}}{\partial t} + \frac{\partial \mathbf{F}_x}{\partial x} + \frac{\partial \mathbf{F}_y}{\partial y} + \frac{\partial \mathbf{F}_z}{\partial z} = \mathbf{H}, \quad (1)$$

which is complemented by the equation of state of the ideal gas

$$p = (\gamma - 1) \rho \left[e - \frac{1}{2} (v_x^2 + v_y^2 + v_z^2 - \omega^2 r^2) \right].$$

The vector of conservative variables \mathbf{Q} and the flow vectors \mathbf{F}_x , \mathbf{F}_y , \mathbf{F}_z have the following form:

$$\mathbf{Q} = \begin{pmatrix} \rho \\ \rho v_x \\ \rho v_y \\ \rho v_z \\ \rho e \end{pmatrix}, \quad \mathbf{F}_x = \begin{pmatrix} \rho v_x \\ \rho v_x v_x + p - \tau_{xx} \\ \rho v_x v_y - \tau_{xy} \\ \rho v_x v_z - \tau_{xz} \\ (\rho e + p) v_x - v_x \tau_{xx} - v_y \tau_{xy} - v_z \tau_{xz} + q_x \end{pmatrix},$$

$$\mathbf{F}_y = \begin{pmatrix} \rho v_y \\ \rho v_y v_x - \tau_{yx} \\ \rho v_y v_y + p - \tau_{yy} \\ \rho v_y v_z - \tau_{yz} \\ (\rho e + p) v_y - v_x \tau_{yx} - v_y \tau_{yy} - v_z \tau_{yz} + q_y \end{pmatrix},$$

$$\mathbf{F}_z = \begin{pmatrix} \rho v_z \\ \rho v_z v_x - \tau_{zx} \\ \rho v_z v_y - \tau_{zy} \\ \rho v_z v_z + p - \tau_{zz} \\ (\rho e + p) v_z - v_x \tau_{zx} - v_y \tau_{zy} - v_z \tau_{zz} + q_z \end{pmatrix}.$$

The noninertiality of the reference system is taken into account by the introduction into the source term \mathbf{H} of the Coriolis and centrifugal forces:

$$\mathbf{H} = \begin{pmatrix} 0 \\ 0 \\ \rho \boldsymbol{\omega} (y\boldsymbol{\omega} + 2v_z) \\ \rho \boldsymbol{\omega} (z\boldsymbol{\omega} - 2v_y) \\ 0 \end{pmatrix}.$$

The tensor components of viscous stresses and the vector components of the heat flow are determined from the relations

$$\tau_{ij} = \mu_{\text{eff}} \left(\frac{\partial v_i}{\partial x_j} + \frac{\partial v_j}{\partial x_i} - \frac{2}{3} \frac{\partial v_k}{\partial x_k} \delta_{ij} \right), \quad q_i = -\lambda_{\text{eff}} \frac{\partial T}{\partial x_i}.$$

Equation (1) is suitable for describing both laminar and turbulent flows. In simulating turbulent flows, it is complemented by the equations of the turbulence model. In so doing, the effective viscosity is calculated as a sum of the molecular and turbulent viscosities, and the effective heat conductivity is expressed in terms of the viscosity and the Prandtl number:

$$\mu_{\text{eff}} = \mu + \mu_t, \quad \lambda_{\text{eff}} = c_p \left(\frac{\mu}{\text{Pr}} + \frac{\mu_t}{\text{Pr}_t} \right).$$

For air, $\text{Pr} = 0.72$, $\text{Pr}_t = 0.9$. To obtain viscosity values depending on the temperature, the Sutherland law is used.

Turbulence Models. To close the Reynolds-averaged Navier–Stokes equations written in the form (1), the Spalart–Allmaras model and the k – ε model of turbulence taking into account the corrections for the rotation and curvature of the streamlines are used.

Spalart–Allmaras model. This model presupposes the solution of the following transfer equation [17] (model SA1):

$$\frac{\partial \rho \tilde{v}}{\partial t} + (\rho \mathbf{v} \cdot \nabla) \tilde{v} = \frac{1}{\sigma} \left\{ \nabla \cdot [(\mu + \rho \tilde{v}) \nabla \tilde{v}] + c_{b2} \rho \nabla \tilde{v} \cdot \nabla (\rho \tilde{v}) \right\} + H. \quad (2)$$

The source term in (2) takes into account the generation and dissipation of the turbulent viscosity

$$H = c_{b1} P \tilde{v} - \left(c_w f_w - \frac{c_{b1}}{\kappa^2} f_{v2} \right) \left(\frac{\tilde{v}}{d} \right)^2.$$

The working variable \tilde{v} is related to the turbulent viscosity as $\nu_t = f_{v1} \tilde{v}$. The turbulence generation term is modeled by the relation

$$P = \tilde{S} f_{v3} + \frac{\tilde{v}}{\kappa^2 d^2} f_{v2},$$

in which \tilde{S} is calculated on the basis of the vortex velocity value

$$\tilde{S} = |\Omega|, \quad |\Omega| = \left(2\Omega_{ij}\Omega_{ij}\right)^{1/2}, \quad \Omega_{ij} = \frac{1}{2}\left(\frac{\partial v_i}{\partial x_j} - \frac{\partial v_j}{\partial x_i}\right).$$

To provide the correct behavior of the working variable in the logarithmic layer ($\tilde{v} = \kappa y u_\tau$), the damping function

$$f_{v1} = \frac{\chi^3}{\chi^3 + c_{v1}}, \quad \chi = \frac{\tilde{v}}{v}.$$

is introduced. The functions f_{v2} and f_{v3} have the following form:

$$f_{v2} = 1 - \frac{\chi}{1 + \chi f_{v1}}, \quad f_{v3} = 1.$$

In the exterior of the boundary layer, an important role is played by the function

$$f_w = g \left(\frac{1 + c_{w3}}{6 + c_{w3}} \right)^{1/6}, \quad g = s + c_{w2} (s^6 - s), \quad s = \frac{\tilde{v}}{\kappa^2 d^2 P}.$$

The function g acts as a limiter, preventing too high values of the function f_w . In so doing, $s = 1$ and $f_w = 1$ in the logarithmic layer, decreasing in the exterior of the boundary layer. The constants of the turbulence model are as follows: $c_{b1} = 0.1355$, $c_{b2} = 0.622$, $\sigma = 2/3$, $c_{v1} = 7.1$, $c_{w1} = c_{b1}/\kappa^2 + (1 + c_{b2})/\sigma$, $c_{w2} = 0.3$, $c_{w3} = 2.0$, and $\kappa = 0.41$.

In the modified Spalart–Allmaras model, the source term is determined by the value of the vortex velocity and the invariant of the strain-rate tensor [18] (model SA2):

$$\tilde{S} = |\Omega| + c_v \min\{0, |S| - |\Omega|\}, \quad |S| = \left(2S_{ij}S_{ij}\right)^{1/2}, \quad S_{ij} = \frac{1}{2}\left(\frac{\partial v_i}{\partial x_j} + \frac{\partial v_j}{\partial x_i}\right),$$

where $c_v = 2.0$.

Dissipative model. The equations of the k – ε model have the form [19]

$$\frac{\partial \rho \tilde{k}}{\partial t} + (\rho \mathbf{v} \cdot \nabla) \tilde{k} = \nabla \cdot \left[\left(\mu + \frac{\mu_t}{\sigma_k} \right) \nabla \tilde{k} \right] + P - \rho \varepsilon, \quad (3)$$

$$\frac{\partial \rho \varepsilon}{\partial t} + (\rho \mathbf{v} \cdot \nabla) \varepsilon = \nabla \cdot \left[\left(\mu + \frac{\mu_t}{\sigma_\varepsilon} \right) \nabla \varepsilon \right] + \frac{\varepsilon}{k} (c_{\varepsilon 1} P - c_{\varepsilon 2} \rho \varepsilon). \quad (4)$$

The turbulence production term is found from the relation (model KE1)

$$P = \mu_t |S|.$$

To take into account the rotation, the Kato–Launder correction [20] (model KE2)

$$P = \mu_t |S|^{1/2} |\Omega|^{1/2}$$

is introduced. The turbulent viscosity is calculated by the Kolmogorov–Prandtl formula $\mu_t = c_\mu \rho k^2 / \varepsilon$. The constants of the turbulence model are $c_\mu = 0.9$, $\sigma_k = 1.0$, $\sigma_\varepsilon = 1.3$, $c_{\varepsilon 1} = 1.44$, and $c_{\varepsilon 2} = 1.92$.

To take into account the curvature of the streamlines, the damping function depending on the turbulent Richardson number [21] (model KE3) is introduced into the turbulent viscosity formula:

$$f_c(\text{Ri}_t) = \frac{1}{1 + c_c \text{Ri}_t},$$

where $c_c = 0.1$ and $0.02 < c_c c_\mu < 0.15$. To calculate the turbulent Richardson number, the formula [22]

$$\text{Ri}_t = \left(\frac{k}{\varepsilon}\right)^2 \left[\frac{|\mathbf{v}|}{W} (\mathbf{b} \cdot \boldsymbol{\Omega}) \right]$$

is used.

Method of Wall Functions. The boundary conditions for the characteristics of turbulence on the wall are set on the basis of the method of wall functions. In the viscous sublayer, viscous stresses dominate over Reynolds stresses, and a linear dependence of the velocity on the distance to the wall $u^+ = y^+$ (at $0 \leq y^+ < 11$) takes place. In the logarithmic layer, Reynolds stresses are much higher than viscous stresses, and the velocity profile is described by the logarithmic law $u^+ = (1/\kappa) \ln(Ey^+)$ (at $11 \leq y^+ < 0.2\delta$). For a smooth wall, $E = 8.8$.

The distribution of shear stresses is assumed to be homogeneous within the limits of the wall control volume. The shear stresses on the wall are calculated by the formula $\tau_w = \mu_{\text{eff}} \Delta u / \Delta y$, where Δu and Δy are the differences of velocities and coordinates between the wall and the wall node. Taking into account that $\mu_{\text{eff}} = \mu \text{Re} / u^{+2}$, where $\text{Re} = \rho \Delta u \Delta y / \mu = u^+ y^+$, we obtain $\tau_w = \rho \Delta u^2 / u^{+2}$.

At $\text{Re} \leq 140$, the velocity distribution is described by the relation

$$0 = u^+ + \left[\exp(\kappa u^+) - 1 - \kappa u^+ - \frac{1}{2} (\kappa u^+)^2 - \frac{1}{6} (\kappa u^+)^3 \right] \exp(-\kappa B) - \frac{\text{Re}}{u^+}. \quad (5)$$

To solve the nonlinear equation (5), the Newton method is used. Iterations begin with $u^+ = \text{Re}^{1/2}$ (in the laminar sublayer $u^+ = y^+$). At $\text{Re} > 140$, the velocity u^+ is found from the logarithmic distribution, which is written in the form

$$y^+ = u^+ + \left[\exp(\kappa u^+) - \kappa u^+ - \frac{1}{2} (\kappa u^+)^2 - \frac{1}{6} (\kappa u^+)^3 \right] \exp(-\kappa B), \quad (6)$$

where $B = 5.3$. Taking the logarithm of (6), we get the relation

$$0 = u^+ - B - \frac{1}{\kappa} \ln \left\{ \exp(-\kappa B) \left[1 + \kappa u^+ + \frac{1}{2} (\kappa u^+)^2 + \frac{1}{6} (\kappa u^+)^3 \right] + \frac{\text{Re}}{u^+} - u^+ \right\}. \quad (7)$$

To solve Eq. (7), the Newton method is used. As the initial approximation, the distribution $u^+ = B + (1/\kappa) \ln \text{Re}$ is used. Relation (7) gives a faster convergence of the Newton method than does expression (6). The same approach is also used to realize the wall-function method for the temperature.

Initial and Boundary Conditions. The angles determining the flow direction are expressed in terms of the velocity components in the cylindrical coordinate system:

$$\alpha = \arctan \frac{v_r}{v_x}, \quad \beta = \arctan \frac{v_\theta}{v_r}.$$

On the inlet boundary of the blade passage we give the total head ($p_0 = 2.7 \cdot 10^5$ Pa), the total temperature ($T_0 = 407$ K), and the turbulent viscosity ($\tilde{\nu}_0 = 10^{-3}$ m²/sec) or the kinetic energy of turbulence and its dissipation rate ($k_0 = 10^{-4}$ m²/sec², $\varepsilon_0 = 10^{-3}$ m²/sec³). The flow is considered to be parallel to the x axis (and $\alpha = \beta = 0$). On the outlet boundary, the static pressure ($p = 1.6 \cdot 10^5$ Pa) is given.

On the inlet boundary of the cavity we give the total head ($p_0 = 1.5 \cdot 10^5$ Pa), the total temperature ($T_0 = 336$ K), the angles determining the flow direction ($\alpha = 90^\circ$, $\beta = 83^\circ$), and the turbulent viscosity ($\tilde{\nu}_0 = 10^{-3}$ m²/sec) or the kinetic energy of turbulence and its dissipation rate ($k_0 = 10^{-4}$ m²/sec², $\varepsilon_0 = 10^{-3}$ m²/sec³).

The no-leakage and adhesion boundary conditions, as well as the temperature ($T_w = 400$ K), are set on the airfoil surface, the blade-passage walls, and the cavity walls. The rate of rotation ($\omega = -1295$ 1/sec) is given on the wall of the cavity formed by the stator surface. The periodic boundary conditions are set in a circular direction.

For the initial conditions, we give the density ($\rho = 1.18$ kg/m³), the static pressure ($p = 2.2 \cdot 10^5$ Pa), and the velocity components ($v_x = 100$ m/sec, $v_y = v_z = 0$). The working medium is air (the thermophysical properties are the reference ones).

Local and Integral Flow Parameters. The flow parameters are calculated in Cartesian coordinates (x, y, z). However, for giving the boundary conditions and processing the results of the numerical simulation, the cylindrical coordinate system (x, r, θ) is also used. The radial and circular velocity components are related to Cartesian components by the relations

$$v_r = \frac{v_y y + v_z z}{(y^2 + z^2)^{1/2}}, \quad v_\theta = \frac{v_z y - v_y z}{(y^2 + z^2)^{1/2}}.$$

The total head loss factor is calculated by the formula

$$L = \frac{p_{01} - p_{02}}{p_{01}},$$

where

$$p_{01} = \frac{1}{A_1} \oint_{A_1} p_0 dA; \quad p_{02} = \frac{1}{A_2} \oint_{A_2} p_0 dA.$$

Indices 1 and 2 correspond to the inlet and outlet cross sections of the calculated region. The rate of flow through the cross section A , whose orientation is defined by the outer normal \mathbf{n} , is calculated by the formula

$$m = \oint_A \rho (\mathbf{v} \cdot \mathbf{n}) dA.$$

Calculations in dimensionless variables makes it possible to join residuals that are due to the discretization of the continuity equations and changes in the momentum and energy (residual R_1), as well as residuals resulting from the discretization of the equations of the turbulence model (residual R_2).

Numerical Method. Discretization of Eq. (1) and the turbulence model equations (2)–(4) is performed by means of the control-volume method [23]. Among the features of the realization of this method are: the possibility of working on both structured and nonstructured meshes; the use of difference schemes having a higher time and spatial coordinate resolution; the choice, for the discretization, of the laws of conservation of the average median control volume; the application of the relations for calculating the gradient and the pseudo-Laplacian that permit obtaining more accurate results on strongly expanded meshes in the boundary layer; and writing the relations for calculating flows through the faces of internal and boundary control volumes in the same form.

For the time discretization, the five-step Runge–Kutta method is used. To discretize nonviscous flows, we use the MUSCL scheme, and for viscous ones — second-order finite-difference formulas.

The system of difference equations is solved by the multimesh method on the basis of the complete approximation scheme. The sequence of embedded meshes is constructed by the method of collapsing faces [23].

The computing procedure was realized in the form of a computer code in the programming languages Fortran 77 and C/C++, and for parallelizing an MPI interface of interprocessor interaction was used.

Results of the Calculations. Calculations were performed on a nonstructured mesh containing 795,038 cells, of which 87,300 cells are located on the boundary. The value of y^+ was varied from 8 to 120.

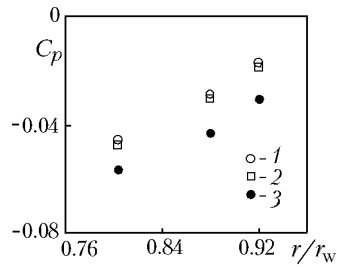


Fig. 2. Radial distributions of the pressure coefficients over the surface of the stationary wall of the cavity: a) $k-\epsilon$ model with a Kato–Lauder correction; 2) Spalart–Allmaras model; 3) data of the physical experiment [12, 13].

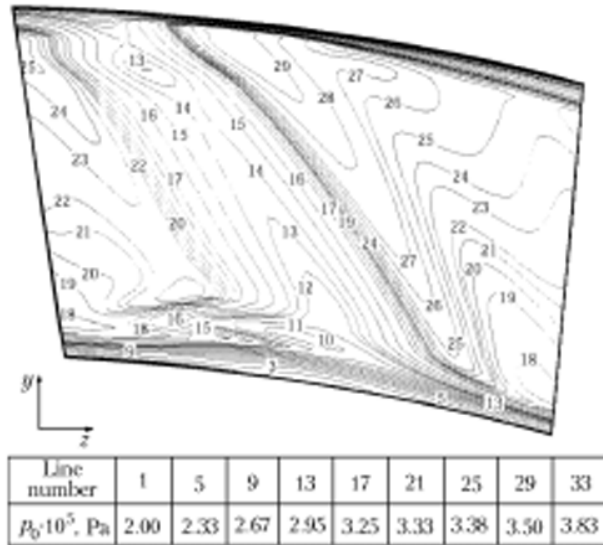


Fig. 3. Lines of the level of the total head in the outlet cross section of the blade passage. The pressure values for the corresponding lines are given in Table 1.

The radial distributions of the pressure coefficient on the wall of the cavity formed by the stator surface are shown in Fig. 2. The pressure coefficient is calculated by the formula

$$C_p = \frac{2 [p(r) - p(r_*)]}{\rho(r_*) (r_w \omega)^2},$$

where τ_w is the cavity radius; r_* , is the *radial coordinate of the reference point* ($r_* = 0.96$). The density at the point $r_* = 0.96$ is calculated by the local values of the pressure and temperature. The dependence of the pressure coefficient on the radial coordinate is close to linear. The results of the calculations are in good agreement with the data of the physical experiment [12, 13], thereby giving a somewhat lower pressure gradient characterized by an inclination of the $C_p(r)$ curve to the abscissa axis. It should be noted that the choice of the turbulence model and the correction for the rotation and curvature of the streamlines have a negligibly small effect on the pressure distribution.

The maximum losses of the total head in the outlet cross section of the blade passage correspond to the region of mixing of the flows behind the rear edge of the airfoil. The results presented in Fig. 3 correspond to the $k-\epsilon$ model with a correction for the curvature of the streamlines (model KE3). The maximum value of the total head in the outlet cross section obtained on the basis of the standard $k-\epsilon$ model (model KE1) is lower compared to the other turbulence models.

TABLE 1. Rates of Flow through Different Cross Sections of the Cavity and Total Head Losses

Model	m_e , kg/sec	$m_{in} \cdot 10^8$, kg/sec	$m_o \cdot 10^2$, kg/sec	$m_c \cdot 10^2$, kg/sec	L, %	R_1	R_2
SA1	4.4548	1.0	2.35	2.48	1.84	-11.16	-15.88
SA2	4.4586	4.0	2.36	2.49	1.85	-10.89	-15.42
KE1	4.4482	1.2	2.55	2.31	3.30	-9.91	-11.17
KE2	4.4518	1.2	2.35	2.31	2.17	-9.76	-11.86
KE3	4.4841	2.2	2.39	2.50	1.39	-11.03	-14.75
[12, 13]	4.4798	$4.8 \cdot 10^3$	1.33	1.27	1.34	-14.56	-16.56

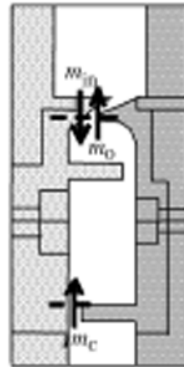


Fig. 4. Rates of flows through different cross sections of the cavity.

The rates of flow through different cross sections of the cavity, the losses of the total head, and the residuals R_1 and R_2 resulting from the discretization of the equations of change in the momentum and the equations of the turbulence model are given in Table 1 (after 60,000 multimesh operations), where m_e is the total rate of flow, m_{in} and m_o are the rates of flow through the inlet and outlet cross sections of the cavity, and m_c is the rate of flow of the cooler (Fig. 4). Unlike the other turbulence models, the level of convergence of the standard $k-\epsilon$ model appears to be unsatisfactory. The introduction of corrections for the rotation and curvature of the streamlines stabilizes numerical calculations.

Comparison of the results with the data of [12, 13] obtained on the basis of the Spalart–Allmaras model (model SA1) but at a smaller value of the flow rate of ingested gas shows that an increase in the flow rate of the cooler by 0.27% leads to a change in the total rate of flow by 0.56% and an increase in the losses by 0.5% of the total head at the inlet to the passage. In so doing, the losses of the total head amount to 2.1% of the kinetic head at the outlet. The dependence of the results of calculations on the choice of the model manifest itself as the fact that the standard $k-\epsilon$ model (model KE1) gives the maximum loss factor compared to the other turbulence models. The results obtained on the basis of the $k-\epsilon$ model with a Kato–Launder correction and without it (models KE1 and KE2) correlate well except for the loss factor (the difference is 51.6%). However, the convergence of the standard $k-\epsilon$ model is much lower than that of the other turbulence models.

The influence of the correction for the streamline curvature is illustrated in Fig. 5, which shows the lines of the kinetic energy level of turbulence in the central cross section of the blade passage (at a constant value of the coordinate $z = 0.16$ m). The kinetic energy level of turbulence remains practically zero in the major part of the calculated region (away from the airfoil). Near the front edge of the airfoil the standard $k-\epsilon$ model, in which the turbulence generation term is calculated on the basis of the invariant of the strain-rate tensor, gives an overstated level of turbulence. The introduction of the Kato–Launder correction permits decreasing the turbulence; nevertheless, its level remains rather high. The overstated kinetic energy level of turbulence is carried downstream and increases as a consequence of the high values of the strain-rate tensor components and the acceleration of the flow along the rarefaction plane of the airfoil. The correction for the streamline curvature suppresses nonphysically the high kinetic energy level of turbulence near the front edge of the airfoil. As a result, the turbulence level remains low throughout the calculated region except for the flow-separation zone.

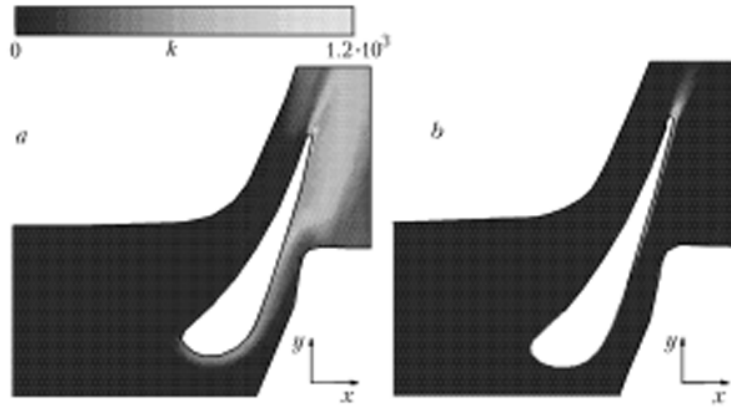


Fig. 5. Lines of the kinetic turbulence energy level in the central cross section of the blade passage: a) k - ϵ model with a Kato-Launders correction; b) k - ϵ model with a correction for the curvature of the streamlines. k , m^2/sec^2 .

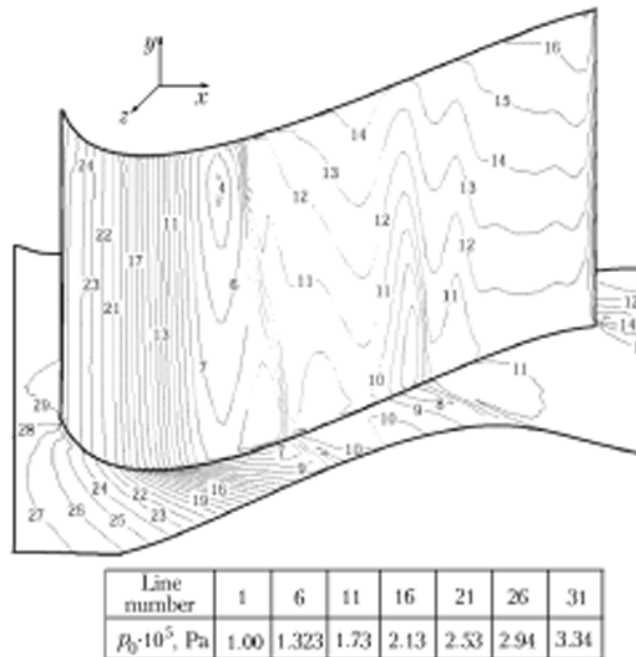


Fig. 6. Lines of the static pressure level on the rarefaction plane of the airfoil. The pressure values for the corresponding lines are given in Table 1.

To understand the structure and the features of the formation and visualization of secondary flows, we use the data on the static pressure (Fig. 6) and surface friction stress (Fig. 7) distributions in the boundary layers formed on the airfoil and on the blade passage walls. The results of the calculations pertaining to the static pressure distribution are almost equal for all turbulence models (the data presented in Fig. 6 correspond to the k - ϵ model with corrections for the streamline curvature). It should be noted that this holds for both the pressure surface and the airfoil rarefaction surface. The results given in Fig. 7 for the airfoil rarefaction surface show the regions of flow with a level of the surface friction stress corresponding to the stagnation of the flow. As a result of the unfavorable pressure gradient in the boundary layer, on the airfoil the boundary layer separates and interacts with the horseshoe vortex formed by the flow separation from the blade passage wall. The calculations with the use of the Spalart-Allmaras model give the lowest level of the surface friction stress, whereas the standard k - ϵ model yields its maximum values. Such behavior can likely be explained by the overstated kinetic energy level of turbulence in the free flow in using the k - ϵ model.

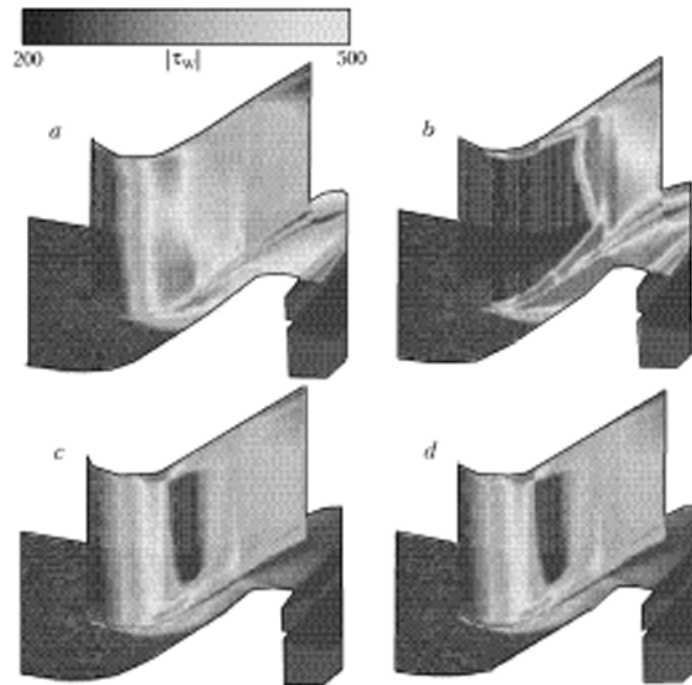


Fig. 7. Lines of the surface friction stress level on the rarefaction plane of the airfoil: a) k - ϵ model with a Kato–Launder correction; b) k - ϵ model with a correction for the curvature of the streamlines; c) Spalart–Allmaras model; d) modified Spalart–Allmaras model. $|\tau_w|$, N/m^2 .

It should be noted that not a single semiempirical model gives flow-separation points (if only the separation point is included in the turbulence model itself). In this connection, an indirect indication of the flow separation is the sharp increase in the friction stress on the airfoil surface. The data presented in Fig. 7 show that the Spalart–Allmaras model and the standard k - ϵ model give the flow separation near the front edge of the airfoil. At the same time, the k - ϵ model with a correction for the curvature of the streamlines gives the flow separation in the central part of the airfoil, which is evidenced by the increase in the surface friction stress in this region.

Interestingly, effects connected with the sensitivity of the surface friction stress distribution to the choice of the turbulence model are observed in using more complex turbulence models, in particular, the SST model and the V2F model [9]. In so doing, the surface friction stress distributions on the airfoil pressure surface demonstrate a weak dependence of the results on the choice of the turbulence model.

The investigation of the topological features of the flow and of the type of special points on the airfoil rarefaction surface and on the blade passage walls shows that near the front edge of the airfoil a saddle point corresponding to the incipience of a horseshoe vortex is formed. The regions of flow with a maximum level of vorticity situated in the vicinity of the front edge of the airfoil on the airfoil rarefaction surface correspond to the region of flow with maximum losses of the total head.

Conclusions. We have investigated the structure and features of the formation of secondary flows in the blade passage of a gas turbine under transverse ingestion of the coolant and compared the results of numerical simulations obtained from the viewpoint of different turbulence models. The introduction of the correction for the curvature of the streamlines stabilizes numerical calculations and improves the convergence of multimesh iterations.

The pressure distribution on the stationary wall of the cavity turns out to be insensitive to the choice of the turbulence model. At the same time, there is a qualitative difference of results pertaining to the surface friction stress distribution over the airfoil rarefaction surface. Unlike the other turbulence models, the k - ϵ model with a correction for the streamline curvature gives a distribution that agrees qualitatively with the data of other investigations.

The mass flow of ingested gas influences the loss of the total head.

NOTATION

A , cross-section area, m^2 ; \mathbf{b} , binormal vector; B , E , constants in the wall law; c_{b1} , c_{b2} , c_v , c_{v1} , c_{w1} , c_{w2} , c_{w3} , constants of the Spalart–Allmaras model; c_c , c_μ , $c_{\epsilon 1}$, $c_{\epsilon 2}$, constants of the dissipative model; c_p , heat capacity at a constant pressure, $J/(kg \cdot K)$; C_p , pressure coefficient; d , distance from the wall, m ; e , total energy of a mass unit, J/kg ; f_c , damping function in the dissipative model; f_{v1} , f_{v2} , f_{v3} , f_w , g , functions in the Spalart–Allmaras model; \mathbf{F} , flow vector; \mathbf{H} , source term; k , kinetic turbulence energy, m^2/sec^2 ; L , total head loss factor, %; m , mass flow, kg/sec ; \mathbf{n} , normal vector; p , pressure, Pa ; P , turbulence generation term, m^2/sec^3 ; Pr , Prandtl number; q , thermal flow, W/m^2 ; \mathbf{Q} , vector of conservative variables; R , residual; Re , Reynolds number; Ri , Richardson number; s , parameter in the Spalart–Allmaras model; S , tensor of strain rates; \tilde{S} , source term in the Spalart–Allmaras model; t , time, sec ; T , temperature, K ; v_x , v_y , v_z , velocity components in the Cartesian coordinate system, m/sec ; v_x , v_r , v_θ , velocity components in the cylindrical coordinate system, m/sec ; \mathbf{v} , velocity vector, m/sec ; W , radius of curvature, m ; x , y , z , Cartesian coordinates, m ; x , r , θ , cylindrical coordinates, m ; α , β , angles giving the flow direction, deg ; γ , ratio between specific heat capacities; δ , thickness of the boundary layer, m ; δ_{ij} , Kronecker symbol; ϵ , dissipation rate, m^2/sec^2 ; κ , Kármán constant; λ , heat conductivity, $W/(m \cdot K)$; μ , dynamic viscosity, $kg/(m \cdot sec)$; ν , kinetic viscosity, m^2/sec ; $\tilde{\nu}$, working variable, m^2/sec ; ρ , density, kg/m^3 ; σ , constant of the Spalart–Allmaras model; σ_k , σ_ϵ , constants of the dissipative turbulence model; τ , shear stress, N/m^2 ; χ , parameter in the Spalart–Allmaras model; ω , angular velocity, $1/sec$; Ω , velocity vortex. Subscripts: c , coolant; e , total; eff , effective; in , inlet cross-section; o , outlet cross-section; t , turbulent; x , y , z , projections on the axis of the Cartesian coordinate system; x , r , θ , projections on the cylindrical coordinate system; w , wall; 0 , drag parameters; $*$, reference point; $+$, dimensionless parameters in the boundary layer.

REFERENCES

1. M. C. Spencer and T. V. Jones, Endwall heat transfer measurements in an annular cascade of nozzle guide vanes at engine representative Reynolds and Mach numbers, *Int. J. Heat Fluid Flow*, **17**, No. 2, 139–147 (1996).
2. N. Aunpapu, R. Volino, K. Flack, and R. Stoddard, Secondary flow measurements in a turbine passage with endwall flow modification, *ASME Paper*, No. GT-2000-0212 (2000).
3. Y. J. Moon and S. R. Koh, Counter-rotating streamwise vortex formation in the turbine cascade with endwall fence, *Comput. and Fluids*, **30**, 473–490 (2001).
4. G. P. Virr, J. W. Chew, and J. Coupland, Application of computational fluid dynamics to turbine disc cavities, *ASME J. Turbomachinery*, **116**, 701–708 (1994).
5. K. Jarzombek, H. J. Dohman, F. K. Benra, and O. Scheider, Flow analysis in gas turbine pre-swirl cooling air systems — variation of geometric parameters, *ASME Paper*, No. GT-2006-90445 (2006).
6. K. Reid, J. Denton, G. Pullan, E. Curtis, and J. Longley, The effect of stator-rotor hub sealing on the main-stream aerodynamics of a turbine, *ASME Paper*, No. GT-2006-90838 (2006).
7. S. Shahpar, D. Giacche, and L. Lapworth, Multi-objective design and optimization of bypass outlet guide vanes, *ASME Paper*, No. GT-2003-38700 (2003).
8. D. Kozulovic and T. Rober, Modelling of streamline curvature effects in turbomachinery flows, *ASME Paper*, No. GT-2006-90265 (2006).
9. R. Pecnik, P. Pieringer, and W. Sanz, Numerical investigation of the secondary flow of a transonic turbine stage using various turbulence closures, *ASME Paper*, No. GT-2005-68754 (2005).
10. C. Cao, J. W. Chew, P. R. Millington, and S. I. Hogg, Interaction of rim seal and annulus flows in an axial flow turbine, *ASME J. Eng. Gas Turbines Power*, **126**, 786–793 (2003).
11. R. Jakoby, K. Lindblad, J. Larsson, L. de Vito, D. Bohn, J. Funcke, and A. Decker, Numerical simulation of the unsteady flow field in an axial gas turbine rim seal configuration, *ASME Paper*, No. GT-2004-53829 (2004).
12. J. Boudet, V. N. D. Autef, J. W. Chew, N. J. Hills, and O. Gentilhomme, Numerical simulation of rim seal flows in axial turbines, *The Aeronaut. J.*, **109**, 373–383 (2005).

13. J. Boudet, N. J. Hills, and J. W. Chew, Numerical simulation of the flow interaction between turbine main annulus and disc cavities, *ASME Paper*, No. GT-2006-90307 (2006).
14. B. Rosic, J. D. Denton, and G. Pullan, The importance of shroud leakage modelling in multistage turbine flow calculations, *ASME Paper*, No. GT-2005-68459 (2005).
15. D. Cherry, A. Wadia, R. Beacock, M. Subramanian, and P. Vitt, Analytical investigation of a low pressure turbine with and without flowpath endwall gaps, seals and clearance features, *ASME Paper*, No. GT-2005-68492 (2005).
16. R. P. Roy, J. Feng, Saurabh P. Narzary, and R. E. Paolillo, Experiments on gas ingestion through axial-flow turbine rim seals, *ASME Paper*, No. GT-2004-53394 (2004).
17. P. R. Spalart and S. R. Allmaras, A one equation turbulence model for aerodynamic flows, *AIAA Paper*, No. 92-0439 (1992).
18. J. Dacles-Mariani, G. G. Zilliac, J. S. Chow, and P. Bradshaw, Numerical/experimental study of a wingtip vortex in the near field, *AIAA J.*, **33**, No. 9, 1561–1568 (1995).
19. B. E. Launder and D. B. Spalding, The numerical computation of turbulent flows, *Comput. Meth. in Appl. Mech. Eng.*, **3**, 269–289 (1974).
20. M. Kato and B. E. Launder, The modelling of turbulent flow around stationary and vibrating square cylinders, in: *Proc. 9th Symp. on Turbulent Shear Flows*, 16–18 August 1993, Kyoto, Japan (1993), Vol. 9, pp. 10.4.1–10.4.6.
21. M. A. Leschziner and W. Rodi, Calculation of annular and twin parallel jets using various discretization schemes and turbulent-model variations, *ASME J. Fluid Eng.*, **103**, 353–360 (1981).
22. A. V. Ermishin and S. A. Isaev (Eds.), *Control of the Flow Past Bodies with Vortical Cells as Applied to Flying Vehicles of Integrated Arrangement (Numerical and Physical Modeling)* [in Russian], Moscow, St. Petersburg (2001).
23. K. N. Volkov, Application of the control-volume method to the solution of problems of fluid mechanics on unstructured grids, *Vychisl. Metody Programmir.*, **6**, No. 1, 43–60 (2005).